High Resolution In-Situ Skin Cancer Microwave Imaging Using Super Wideband Antenna

Wasan Alamro, Boon-Chong Seet
Dept. of Electrical & Electronic Engg.
Auckland University of Technology
Auckland, New Zealand

Lulu Wang
Biomedical Device Innovation Center
Shenzhen Technology University
Shenzhen, China

Prabakar Parthiban
Hardware Engineering Department
Honeywell Aerospace
Yeovil, UK

Abstract—**This paper investigates the capability of a super wideband (SWB) antenna based imaging system in early-stage skin cancer detection. The imaging system consists of eight antenna elements in a circular array positioned around a human trunk phantom modeled as five concentric layers of skin, fat, muscle, rib bone and lung tissues. The dielectric properties of the phantom tissues are calculated using Cole-Cole model. The skin tumor is modeled as cylindrical shape on the outer skin layer with 1mm thickness and 15mm diameter. The resulting S-parameters of healthy and malignant phantoms obtained over different frequency ranges are compared and used to reconstruct the 2D images of the trunk area. The results show that the proposed SWB imaging system can detect and localize in-situ skin cancer with relatively high accuracy.**

Keywords-High Resolution; In-Situ; Skin Cancer; Microwave Imaging; Super Wideband; Antenna

I. INTRODUCTION

Melanoma is a serious and malignant type of skin cancer, and New Zealand has one of the highest rates of cutaneous melanoma in the world in terms of both occurrence and fatality [1]. Human trunk, i.e. chest and back, is the site of the body with the highest occurrence of melanoma especially in men [2]. Melanoma has different stages: from stage 0 or in-situ stage where the tumor is on the skin's outermost layer (epidermis) to stage 4 where the tumor has spread beyond lymph nodes to other organs. During in-situ melanoma stage, the tumor has not spread to lymph nodes and has no more than 1 mm thickness. In recent years, microwave imaging has attracted much interest as a noninvasive detection technique for different cancer types and for frequent monitoring after a curative procedure, due to its capability in detecting the presence of cancer lesions, high safety, and low cost [3].

A number of research has been conducted on microwave imaging techniques for skin cancer [4-8]. Four antipodal Vivaldi antennas with distinct sub-bands are presented in [4]. Collectively, the antennas provide an overall bandwidth of 98 GHz with 10 to 12 dBi gain. The proposed imaging system was tested on one layer skin phantom with 2mm thickness. Two droplet tumors with 400 μm diameter were embedded at 1mm depth inside the phantom. Imaging results show high resolution in detecting both tumors, but the performed measurements had considered only the effect of skin layer in the imaging setup. Moreover, unlike other types of tumors, the skin tumor starts on the outer skin layer, not below it. In [5], an ultra-wideband (UWB) antenna of 5.72 GHz bandwidth and 6.4 dBi gain is proposed for in-vitro skin cancer detection. The proposed antenna is tested on 100 mm diameter forearm phantom with four layers (skin, fat, muscle, and bone). Imaging results show a successful detection of 20 mm diameter tumor placed on the outer skin layer with 2 mm thickness. However, only one antenna is used during measurement with manual placements at different positions around the phantom. A wearable UWB antenna integrated with artificial magnetic conductor (AMC) is presented in [6]. The proposed antenna is tested on a three-layer phantom consisting of skin, fat and muscle. The simulated S-parameters result show discrepancy between healthy and cancerous tissues. However, the tumor size, thickness and the imaging results are not discussed. An UWB imaging method applied to a forearm phantom of three layers: cortical bone, adipose-muscle and skin tumor, is presented in [7]. Although successful in detecting the skin tumor, the skin layer presented is using an external plastic cylinder with tumor contained inside the adipose layer. In [8], an elliptical UWB antenna with stub loading to shift the frequency to lower bands is presented. The antenna operates in the frequency range from 3.9 to 30 GHz with peak gain of 6.48 dBi. A semi-spherical array arrangements of nine antenna elements is placed around a fabricated breast phantom consisting of skin and fat layers for tumor detection in the breast skin. A 4 mm diameter tumor placed at the boundary of skin and fat layers is successfully detected. However, the used phantom is a simplified one without representation of the tumor thickness and placement in the outer skin layer.

From the above reviews, it can be seen that except for one, all previous works detect skin tumor located at some depth of the skin layer or even lower in the adipose layer. In this paper, we investigate the capability of a microwave imaging system with an array of eight SWB antenna elements to accurately detect in-situ skin tumor of smaller diameter and thickness than those in prior state-of-the-art. We developed our own custom SWB antenna whose original design is reported in [9], but has been modified to achieve a super wide bandwidth of 32.9 GHz.

II. PHANTOM MODELING FOR SKIN CANCER DETECTION

In this section, we modeled a human trunk phantom with tumor lesion using a cylindrical structure consisting of six tissue layers (skin, fat, muscle, cancellous bone, lung and skin cancer inclusion). The modeled phantom mimics an adult size torso with a perimeter of 82.3 cm. The skin tumor is further modeled as a cylindrical disc of 7.5 mm radius, 1 mm thickness, and embedded at a depth of 1mm below the external skin tissue. Fig. 1 shows the structure and dimensions of our phantom. A simulated study is performed using Ansys HFSS where eight SWB antenna elements are

positioned uniformly around the phantom and at a distance of 10 mm away from the skin layer as shown in Fig. 2. The skin tumor is placed near to Antenna 1. The dielectric properties of each phantom layer are calculated using the Cole-Cole model [10] and listed in Table I. The properties are calculated at a frequency of 7.8 GHz, which corresponds to the second resonant frequency of our SWB antenna, and where the signal wavelength provides suitable penetration depth for skin cancer detection while not incurring excessive frequency-related attenuation.

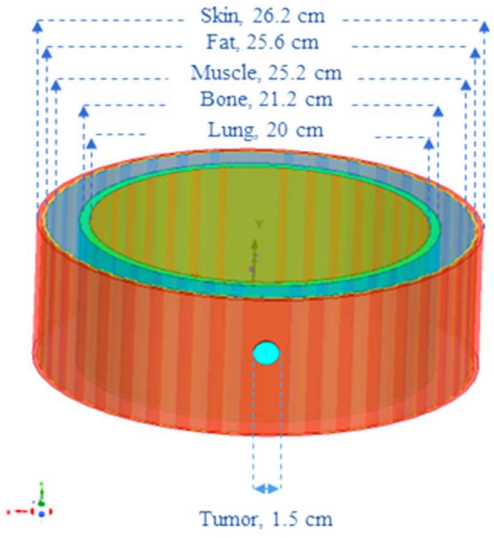

Figure 1. Human trunk phantom with tumor lesion on skin tissue.

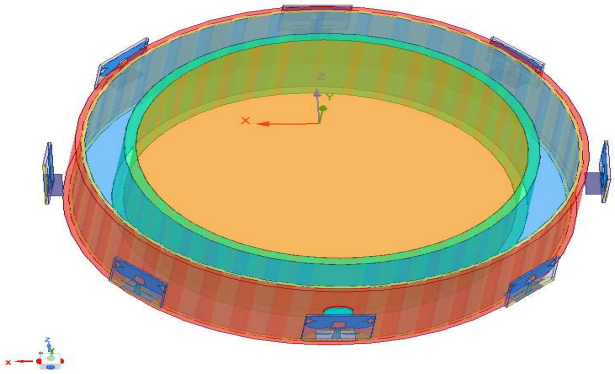

Figure 2. SWB antenna array positioned around phantom with 45˚ separation.

TABLE I. DIELECTRIC PROPERTIES OF TRUNK PHANTOM WITH TUMOR

Tissue	Cole-Cole Dielectric Properties at 7.8 GHz		
	Relative Permittivity ε_r	*Conductivity σ (S/m)*	*Loss tangent tanδ*
Skin	33.36	5.6	0.388
Fat	9.32	1.24	0.306
Muscle	45.74	7.55	0.379
Cancellous bone	13.95	2.98	0.492
Inflated Lung	17.36	3.05	0.405
Tumor	51.01	9.67	0.437

III. S-PARAMETERS RESULTS

In this section, we present a comparison between simulated S-parameters of the healthy phantom (without skin tumor) and unhealthy phantom (with skin tumor). It should be noted that the dielectric properties of cancerous tissue would tend to be higher than those of normal tissues, due to the higher water and oil content in the malignant lesions. Fig. 3 shows the magnitude of reflection coefficients ($|S_{11}|..|S_{88}|$) from all eight antennas, while Fig. 4 shows their zoomed-in responses at 3.8 GHz, 7.8 GHz, and 14.8 GHz, which represent the first, second, and third resonant frequencies of the antenna, respectively. It can be observed that the unhealthy phantom shows higher reflection compared to the healthy phantom at all three resonant frequencies. The largest observed difference in reflection response between healthy and unhealthy phantoms is ~ 6.8 dB, attributed by Antenna 1, i.e. the antenna nearest to and facing the cancerous lesion; and expectedly occurs at the second resonant frequency (same frequency for calculating the phantom's dielectric properties). This difference in reflection response is due to the significant influence of constituent water content in the malignant lesions.

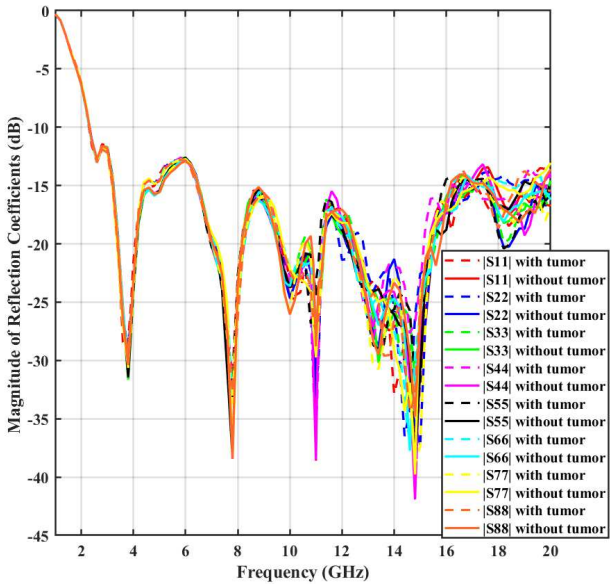

Figure 3. Magnitude of reflection coefficients of all eight antennas from healthy and unhealthy phantoms

Fig. 5 shows the corresponding magnitude of transmission coefficients, which reflect the degree of undesired mutual coupling between antenna elements in the circular array. For improved presentation, we plotted only forward transmission coefficients from all but one array elements (Antenna 2, 3, ..8) to Antenna 1, since the reversed transmission coefficients from Antenna 1 to all other array elements are found to exhibit a similar performance trend. It is observed that a low mutual coupling of below -30 dB, i.e. good isolation between array elements, is preserved over the entire covered bandwidth. Comparing between the healthy and unhealthy phantom, it is also evident that the transmission coefficients in the case of healthy phantom are slightly better (implying lower loss). This observation is consistent with the known effect of tumor lesion, which is the high scattering of signals.

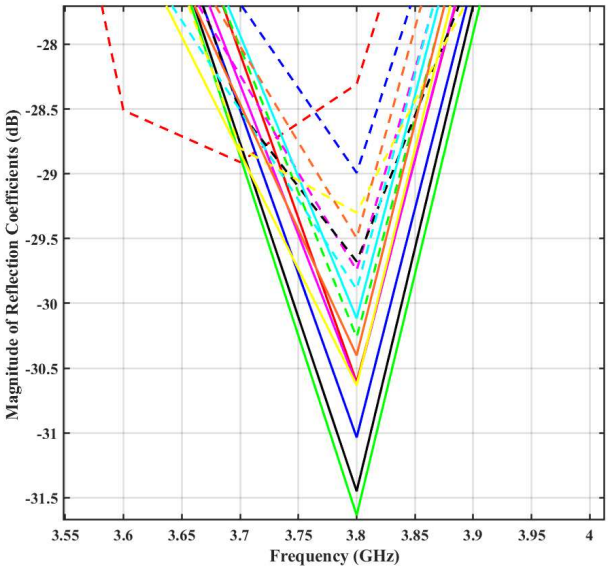

(a)

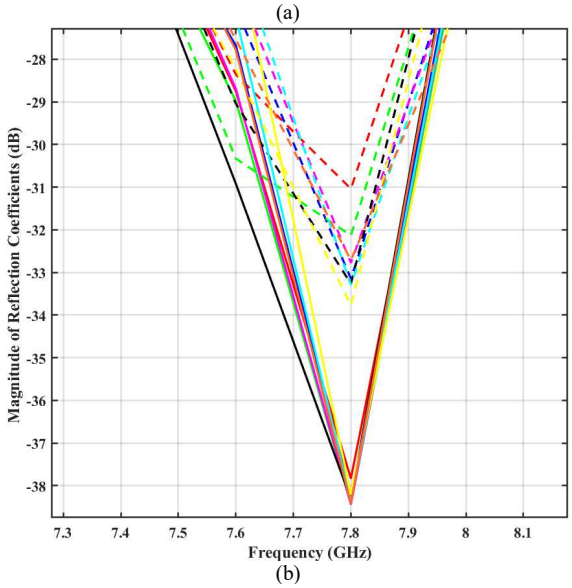

(b)

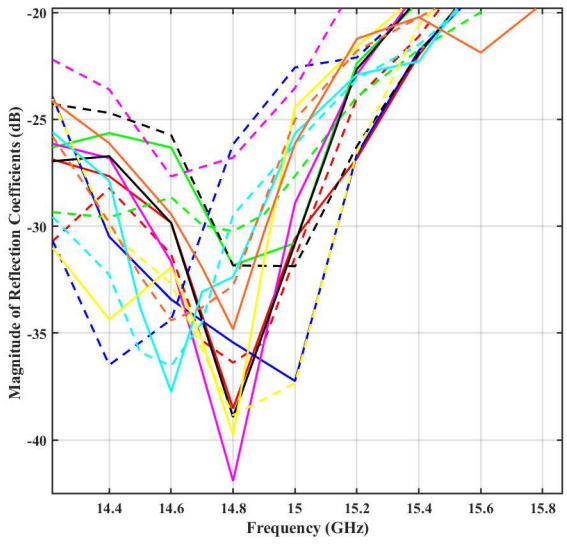

(c)

Figure 4. Zoomed-in reflection response at: (a) 3.5 GHz; (b) 7.8 GHz; and (c) 14.8 GHz.

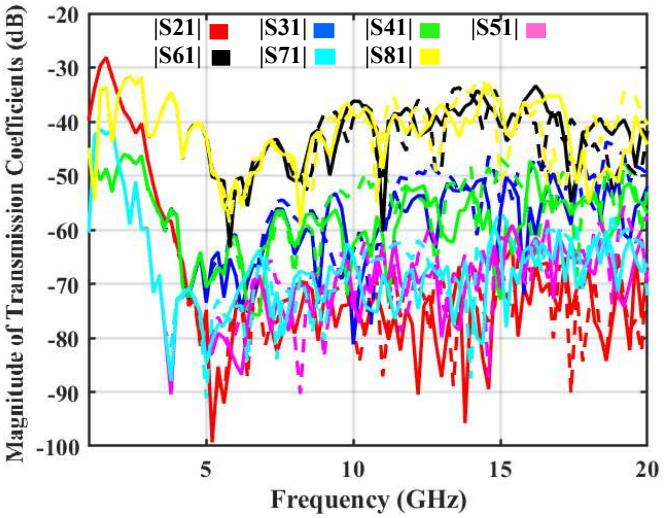

Figure 5. Magnitude of transmission coefficients from all eight antennas in healthy (solid line) and unhealthy (dashed line) phantoms.

IV. IMAGE RECONSTRUCTION

In this section, 2D images of the trunk phantom are generated using the delay-multiply-and-sum (DMAS) algorithm, which is a beamforming confocal imaging algorithm known to be able to localize malignant lesion accurately while reducing background clutter [11]. This technique is based on antenna pair multiplication before the summation of reflected signals measured at different antenna positions. The obtained S-parameters are processed using DMAS and an artefact removal technique described by (1):

$$s_m(t) = x_m^U(t) - x_m^H(t) \quad (1)$$

where $s_m(t)$ is the resultant reflected signal after the artefact removal, $x_m^U(t)$ and $x_m^H(t)$ are the recorded signals from the unhealthy phantom, and healthy phantom, respectively.

The artefact usually consists of reflections of the incident wave from the interface between the skin and trunk, and some residual antenna reverberation. Failure to eliminate this artefact could mask tumors that may be present in the skin, resulting in unsuccessful detection. A commonly employed signal preprocessing method for artefact removal is to perform a subtraction between two sets of S-parameter data: one acquired under no tumor (healthy phantom); and the other acquired under tumor (unhealthy phantom). This eliminates the common background clutter from the two datasets, resulting in enhanced tumor response.

The reconstructed image can be generated using (2):

$$I(r) = \sum_{m=1}^{M-1} \sum_{n=m+1}^{M} s_m[t_m(r)].s_n[t_n(r)] \quad (2)$$

where $I(r)$ is the intensity value at point r (position of pixel in the phantom space), M is the number of antenna positions used in the scan, s_m is the delayed reflected signal measured at m^{th} position, s_n is the delayed paired signal of s_m measured at n^{th} position. In this process, the delayed reflected and paired signals are multiplied before being summed. This increases the sample size, which leads to improved clutter reduction, but also longer computation time. The $t_m(r)$ and $t_n(r)$ are the time-of-flight of s_m, and s_n, respectively, as defined in (3), $\boldsymbol{r}_m$ and $\boldsymbol{r}_n$ are the m^{th}, and n^{th}antenna position, respectively, and v is the average signal propagation speed of in the phantom space.

$$t_m(r) = 2\frac{|r - r_m|}{v} \quad (3a)$$

$$t_n(r) = 2\frac{|r - r_n|}{v} \quad (3b)$$

The image reconstruction process is implemented on both healthy and unhealthy phantoms. Fig. 6 shows the reconstructed image of the healthy phantom where X and Z are the image axes, corresponding to the horizontal plane, and vertical plane in the phantom space, respectively.

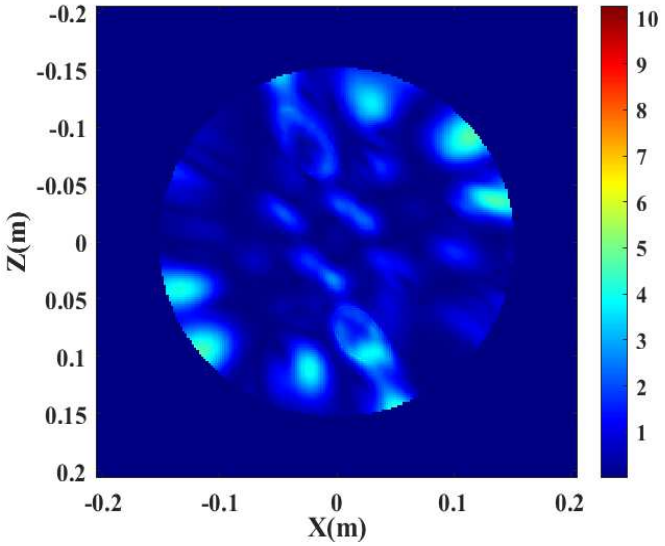

Figure 6. Reconstructed image of healthy phantom using S-parameters obtained in the frequency range of 2.5–20 GHz.

The images of the tumor lesions in unhealthy phantom are obtained using simulated S-parameter data. The image in Fig. 7 is using S-parameters acquired over a relatively small covered bandwidth of 7.5 GHz in the frequency range of 2.5–10 GHz. The detected tumor in this scenario is 17.3 mm in diameter and 1.4 mm thickness below the skin layer. Another image in Fig. 8 is using S-parameters acquired over a wider covered bandwidth of 17.5 GHz in the frequency range of 2.5–20 GHz. It is generated with enhanced clutter removal and improved resolution due to the bandwidth enlargement. The detected tumor in this scenario is 16 mm in diameter and 1.3 mm thickness below the skin layer. The center of the detected tumor is estimated to be located at (0, 154.3) mm in both scenarios.

The actual diameter, thickness, and location of the tumor are 15 mm, 1 mm, and (0, 154.5) mm, respectively. The corresponding percentage errors are calculated as shown in Table II. It can be observed that both scenarios could result in successful tumor detection and localization. However, utilizing a wider covered bandwidth and higher frequency data points expectedly results in better image resolution and consequently more accurate estimation in terms of the tumor's diameter and thickness.

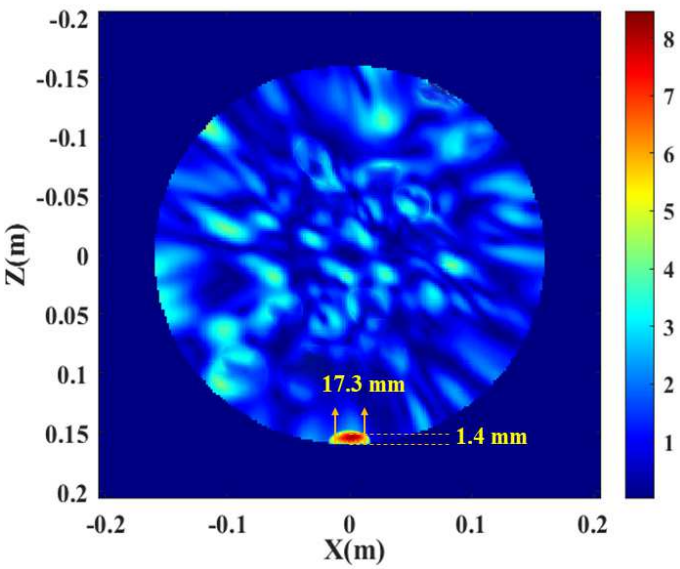

Figure 7. Reconstructed image of unhealthy phantom using S-parameters obtained in the frequency range of 2.5–10 GHz.

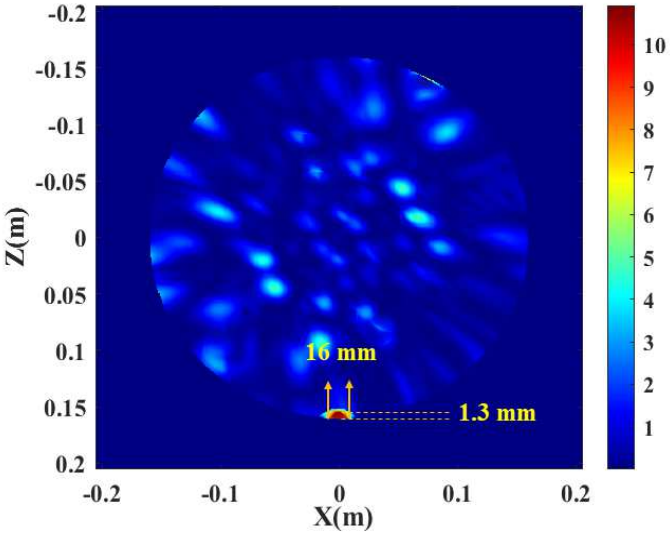

Figure 8. Reconstructed image of unhealthy phantom using S-parameters obtained in the frequency range of 2.5–20 GHz.

TABLE II. PERCENTAGE ERROR

Parameter	*Covered bandwidth*	*Estimated result*	*Absolute error*	*Percentage error*
Diameter	17.5 GHz	16 mm	1 mm	6.66%
	7.5 GHz	17.3 mm	2.3 mm	15.33%
Thickness	17.5 GHz	1.3 mm	0.3 mm	30%
	7.5 GHz	1.4 mm	0.4 mm	40%
Location	17.5 GHz	(0, 154.3) mm	(0, 0.2) mm	0.13%
	7.5 GHz			

V. CONCLUSION

In this paper, we investigated the capability of a SWB antenna array system in detecting in-situ skin cancer through S-parameter

analysis and microwave imaging with high resolution. The analysis of the S-parameter results shows notable differences between the backscattered signals from healthy and unhealthy phantoms due to the dielectric contrast. The proposed system shows promising results in detecting and localizing early-stage skin tumor with 15 mm diameter and 1 mm thickness. In future work, a real experimental measurement will be conducted on a fabricated trunk phantom that mimics the dielectric properties of human tissues across a super wide bandwidth in the frequency range from 2.5–35.4 GHz.

ACKNOWLEDGMENT

This research was funded by the International Science and Technology Cooperation Project of the Shenzhen Science and Technology Innovation Commission (GJHZ20200731095804014).

REFERENCES

[1] J. Z. Lim, S. L. Misra, A. Gokul, P. W. Hadden, A. Cavadino, and C. N. McGhee, ''Conjunctival Melanoma in Aotearoa—New Zealand: A 21-Year Analysis of Incidence and Survival,'' The Asia-Pacific Journal of Ophthalmology, vol. 12(3), 2023, pp. 273-278.

[2] N. Pandeya, C. M. Olsen, M. M. Shalit, J. C. Dusingize, R. E. Neale, and D. C. Whiteman, ''The diagnosis and initial management of melanoma in Australia: findings from the prospective, population-based QSkin study,'' Medical Journal of Australia, 2023.

[3] W.H. Al Amro, and B-C. Seet, ''Review of practical antennas for microwave and millimetre-wave medical imaging,'' In Electromagnetic Waves and Antennas for Biomedical Applications, 1st ed., Wang, L. Eds., IET The Institution of Engineering and Technology: UK, 2021, pp. 185-207.

[4] A. Mirbeik-Sabzevari, et al., ''Synthetic ultra-high-resolution millimeter-wave imaging for skin cancer detection,'' IEEE Transactions on Biomedical Engineering, vol. 66(1), 2018, pp. 61-71.

[5] K. Kaur, and A. Kaur, ''In vitro detection of skin cancer using an UWB stacked micro strip patch antenna with microwave imaging,'' Int J RF Microw Comput Aided Eng., 2022, e23407. doi:10.1002/mmce.23407

[6] A.M. Tripathi, P.K. Rao, and R. Mishra, ''An AMC inspired wearable UWB antenna for skin cancer detection,'' in 2020 International Conference on Electrical and Electronics Engineering (ICE3), 2020, IEEE.

[7] B. Khalesi, G. Tiberi, N. Ghavami, M. Ghavami, and S. Dudley, ''Skin cancer detection through microwaves: validation on phantom measurements,'' IEEE., vol. 1, 2018, pp. 1-6.

[8] S. Alani, Z. Zakaria, T. Saeidi, A. Ahmad, M. A. Imran, and Q. H. Abbasi, ''Microwave imaging of breast skin utilizing elliptical UWB antenna and reverse problems algorithm,'' Micromachines, vol. 12(6), 2021, pp. 647. doi:10.3390/mi12060647

[9] W. A. Alamro, B. -C. Seet, L. Wang and P. Parthiban, ''Compact Super-Wideband Antenna for Medical Imaging Applications,'' 2021 IEEE Conference on Antenna Measurements & Applications (CAMA), Antibes Juan-les-Pins, France, 2021, pp. 505-508, doi: 10.1109/CAMA49227.2021.9703550.

[10] A. Mirbeik-Sabzevari, N. Tavassolian, ''Ultrawideband, stable Normal and cancer skin tissue phantoms for millimeter-wave skin cancer imaging,'' IEEE Trans Biomed Eng., vol. 66, 2019, pp. 176-186.

[11] M. A. Elahi, D. O'Loughlin, B. R. Lavoie, M. Glavin, E. Jones, E. C. Fear, and M. O'Halloran, ''Evaluation of image reconstruction algorithms for confocal microwave imaging: Application to patient data,'' Sensors, vol. 18(6), 2018, pp. 1678.